Transient carrier dynamics in a Mott insulator with antiferromagnetic order

Eiki Iyoda* and Sumio Ishihara

Department of Physics, Tohoku University, Sendai 980-8578, Japan, and JST-CREST, Sendai 980-8578, Japan

(Received 4 December 2013; revised manuscript received 9 March 2014; published 27 March 2014)

We study transient dynamics of hole carriers injected into a Mott insulator with antiferromagnetic long-range order. This "dynamical hole doping" contrasts with chemical hole doping. The theoretical framework for the transient carrier dynamics is presented based on the two-dimensional t-J model. The time dependencies of the optical conductivity spectra, as well as the one-particle excitation spectra, are calculated based on the Keldysh Green's function formalism at zero temperature combined with the self-consistent Born approximation. In the early stage after dynamical hole doping, the Drude component appears, and then incoherent components originating from hole-magnon scattering start to grow. Fast oscillatory behavior owing to coherent magnon and slow relaxation dynamics are confirmed in the spectra. The time profiles are interpreted as doped bare holes being dressed by magnon clouds and relaxed into spin polaron quasiparticle states. The characteristic relaxation times for Drude and incoherent peaks strongly depend on the momentum of the dynamically doped hole and the exchange constant. Implications for recent pump-probe experiments are discussed.

DOI: 10.1103/PhysRevB.89.125126 PACS number(s): 71.27.+a, 78.47.J−, 71.30.+h, 78.20.−e

I. INTRODUCTION

Ultrafast carrier dynamics in strongly correlated electron systems has attracted significant attention because of the number of time-resolved experimental techniques that have been rapidly developed in the past decade. In contrast to conventional metals and semiconductors, correlated electron systems show a rich variety of competing phases, interactions, and degrees of freedom. Intensive external stimuli, such as a short laser pulse, or dc or ac electric fields, can trigger the breaking of the subtle balance between them and often induce some nontrivial transient states, which are never realized in thermal equilibrium states. Numerous experiments and theoretical analyses on transient carrier dynamics have been done in several classes of correlated electron systems, e.g., charge-ordered organic salts, spin crossover complexes, magnetic oxides, multiferroics, and superconducting materials [1,2].

It is widely recognized that one of the prototypical and yet unrevealed issues in transient electron dynamics is photoirradiation effects in a Mott insulator with antiferromagnetic long-range order (AFLRO). This is motivated not only by the deep understanding of Mott insulators and high-transition-temperature superconductivity, but also by a search for drastic photoinduced nonequilibrium states [3–9]. The optical pump-and-probe experiment is a standard method in which transient electron and hole dynamics excited across a Mott gap are directly detected [10–22]. Ultrashort optical pulses have revealed the real-time dynamics of electrons and holes and their relaxations toward recombination and thermalization. Recent pump-probe experiments in quasi-two-dimensional Mott insulators, as parent compounds of high-transition-temperature superconductivity, revealed that a metallic Drude component appears just after photoexcitation and decays within several tens of femtoseconds [23]. After several picoseconds, the midgap absorptions appear, and two absorption peaks are separately identified as hole and electron carrier contributions. These systematic experimental observations require a detailed understanding of the carrier dynamics doped temporally into a Mott insulator with AFLRO [24].

In this paper, we examine the real-time dynamics of hole carriers introduced into a Mott insulating state with AFLRO. This doping is termed "dynamical hole doping," and the introduced holes are "dynamically doped holes," in contrast with chemically doped holes (see Fig. 1). The concept of dynamical hole doping, not electron-hole pairs, not only is advantageous for a simple theoretical setup, but also has implications for recent optical pump-probe experiments, where the dynamics of photodoped holes and electrons were observed separately [23,25–28]. We present the theoretical framework for the dynamically doped holes based on the two-dimensional t-J model. We adopt the Keldysh Green's function formalism [29–31] and the self-consistent Born (SCB) approximation [32,33], the latter of which is known to describe well motions of chemically doped holes in a Mott insulator with AFLRO. To examine real-time dynamics of dynamically doped holes, the transient optical conductivity spectra, as well as the one-particle excitation spectra, are calculated. In the early stage after hole doping, only the Drude component appears in the optical conductivity spectra, and then incoherent peaks originating from hole-magnon scattering start to grow. The intensities of these peaks during the early stage are proportional to t^2 and t^3, where t represents time. Fast oscillatory behavior, owing to coherent magnon, and slow relaxation dynamics are confirmed in the spectra. The time profiles are interpreted as the results of doped bare holes being dressed by magnon clouds and relaxed into spin polaron quasiparticles (QPs) in the steady state. We show that the relaxation time scales strongly depend on the momentum of the dynamically doped hole and the magnitude and anisotropy of the exchange constant.

In Sec. II, the t-J model represented by spinless fermion and spin-wave operators are introduced. In Sec. III, we present the theoretical formalism for the real-time dynamics of doped

*Present address: Department of Basic Science, The University of Tokyo, 3-8-1 Komaba, Meguro-ku, Tokyo 153-8902 Japan; iyoda@noneq.c.u-tokyo.ac.jp

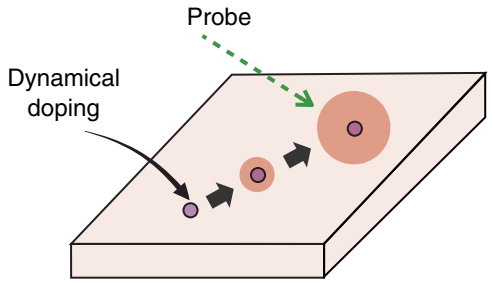

FIG. 1. (Color online) Schematic of dynamical hole doping.

holes based on the Keldysh Green's function and the SCB approximation. Numerical results of transient hole dynamics are given in Sec. IV. Section V is devoted to the conclusion. In the Appendix, we present the dominant pole approximation (DPA), adopted to analyze the numerical results in Sec. IV.

II. MODEL

We start from the t-J model in a two-dimensional square lattice given by

$$\mathcal{H} = -t_0 \sum_{\langle ij\rangle\sigma} (\tilde{c}^\dagger_{i\sigma}\tilde{c}_{j\sigma} + \text{H.c.}) + \sum_{\langle ij\rangle}\left\{ J_\parallel S^z_i S^z_j + \frac{J_\perp}{2}(S^+_i S^-_j + S^-_i S^+_j)\right\}, \quad (1)$$

where $\tilde{c}_{i\sigma} = c_{i\sigma}(1-n_{i-\sigma})$ is the annihilation operator for an electron with spin $\sigma(=\uparrow,\downarrow)$ at site i without double occupancy, and $\mathbf{S}_i$ is a spin operator with an amplitude of $S = 1/2$. The transfer integral is represented by t_0 to distinguish it from the symbol for time. For convenience, we introduce anisotropy into the exchange interaction as a parameter $\alpha \equiv J_\perp/J_\parallel$; $\alpha = 1$ ($\alpha = 0$) corresponds to the Heisenberg (Ising) limit.

We assume an AFLRO state in the ground state, where sublattices for up- and down-spins are termed A and B, respectively. Spin operators are represented by magnon operators introduced by the Holstein-Primakov transformation as $S^+_i = (1-a^\dagger_i a_i)^{1/2} a_i$, $S^-_i = a^\dagger_i (1-a^\dagger_i a_i)^{1/2}$, and $S^z_i = 1/2 - a^\dagger_i a_i$ for sublattice A and in similar ways for sublattice B. Following Refs. [32] and [33], the electron operator without double-occupancy is given by the slave fermion representation as $\tilde{c}^\dagger_{i\sigma} = h_i a^\dagger_{i\sigma}$ with the constraint $\sum_\sigma a^\dagger_{i\sigma} a_{i\sigma} + h^\dagger_i h_i = 1$, where h_i is a spinless fermion operator for a hole. Up to the lowest order of the $1/S$ expansion, where $a_{i\in A\downarrow}$ and $a_{i\in B\uparrow}$ are replaced by $\sqrt{2S}(=1)$, the hopping term of the Hamiltonian is given as

$$\mathcal{H}_t = -t_0 \sum_{\langle ij\rangle i\in A j\in B} h_i h^\dagger_j (a^\dagger_{i\uparrow} + a_{j\downarrow}) + \text{H.c.} \quad (2)$$

The J term expressed by the bilinear form of the boson operator is diagonalized by the Bogoliubov transformation.

By introducing the Fourier transformation, the Hamiltonian is finally given by

$$\mathcal{H}_t = \frac{z t_0}{\sqrt{N}} \sum_{\boldsymbol{k},\boldsymbol{q}} h^\dagger_{\boldsymbol{k}} h_{\boldsymbol{k}-\boldsymbol{q}} \alpha_{\boldsymbol{q}} M_{kq} + \text{H.c.} \quad (3)$$

for the t term, with coupling constant

$$M_{kq} = u_q \gamma_{k-q} + v_q \gamma_k, \quad (4)$$

and by

$$\mathcal{H}_J = \sum_{\boldsymbol{q}} \omega_{\boldsymbol{q}} \alpha^\dagger_{\boldsymbol{q}} \alpha_{\boldsymbol{q}} \quad (5)$$

for the J term. Here, $\alpha_{\boldsymbol{q}}$ is a boson operator for the magnon introduced by the Bogoliubov transformation, and $h_{\boldsymbol{q}}$ is the Fourier transform of h_i. We define the magnon dispersion $\omega_q = zJS(1-\delta_d)^2 v_q$, where δ_d is the hole density, $S = 1/2$, and $v_q = [1-(\alpha\gamma_q)^2]^{1/2}$, with the form factor $\gamma_q = (\cos q_x + \cos q_y)/2$ and the coordination number z (=4). The factors u_q and v_q in M_{kq} are given by the usual expression in the Bogoliubov transformation, defined by $u_q = [(1+v_q)/(2v_q)]^{1/2} v_q = -\text{sgn}(\gamma_q)[(1-v_q)/(2v_q)]^{1/2}$. As is well known, there is an absence of the kinetic term of $\sum_{\langle ij\rangle} h^\dagger_i h_j$, and the coupling M_{kq} between a fermion and magnons in the t term is the source of the hole dynamics. Henceforth, we adopt units of energy and time as t_0 and t_0^{-1}, respectively.

III. FORMULATION

A. Initial state and Keldysh formalism

We explain the situation for dynamical hole doping and how to observe transient states. First, a hole is introduced into the Néel ordered state at half-filling by an external field at $t = 0$. This state is adopted as an initial state and is simulated by

$$|i\rangle = \sum_{k_i} f(k_i) h^\dagger_{k_i} |0\rangle, \quad (6)$$

where $|0\rangle$ expresses the Néel state (termed the "vacuum" state). The function $f(k_i)$ describes the momentum distribution of a doped hole and its functional form depends on the actual hole-injection method.

This initial state is time-evolved by the Hamiltonian $\mathcal{H}_t + \mathcal{H}_J$ given in Eqs. (3) and (5). At time $t > 0$, the expectation value of an operator is defined as

$$\langle O(t)\rangle = \langle i|O_H(t)|i\rangle, \quad (7)$$

where $O_H(t)$ is its Heisenberg representation. To use Wick's theorem, we introduce the Keldysh's closed-time contour whose length is finite, as shown in Fig. 2. Then $\langle O(t)\rangle$ is given by

$$\langle O(t)\rangle = \sum_{k_i} f(k_i)^2 \langle 0|T_C\left\{U_C h_{k_i}(0^<_c) O(t^<_c) h^\dagger_{k_i}(0^>_c)\right\}|0\rangle, \quad (8)$$

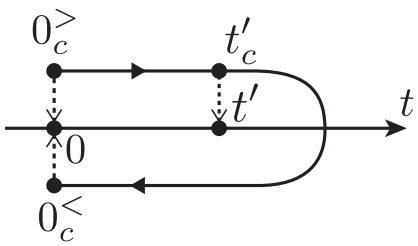

FIG. 2. A Keldysh contour.

with

$$U_C = T_C \exp\left(\int_C -i\mathcal{H}_t(t_c')dt_c' \right), \tag{9}$$

where all time-dependent operators are represented in the interaction representation. The time variable on a Keldysh contour is denoted t_c with subscript c, and a projection of t_c onto the real-time axis is t. The superscript $>$ ($<$) indicates that the contour time is on the upper (lower) branch of the Keldysh contour. The symbol T_C is a Keldysh contour ordering operator, and $\int_C$ implies an integral along the contour. We have relations $0_c^< >_K t_c$ and $0_c^> <_K t_c$ for any t_c, where $<_K$ and $>_K$ represent inequalities defined on the Keldysh contour. Wick's theorem and Feynman's rules are applicable to this form of the expectation value. We note that the imaginary contour from $t = 0$ to $-i/(k_B T)$, known as the Kadanoff-Baym's L-shaped contour, does not need to be taken into account in the present formalism. This is because the initial state is explicitly given in Eq. (6), and thermal equilibrium processes along the imaginary contour are not necessary.

B. Green's function

In the Keldysh formalism, the one-particle Green's function (nonequilibrium Green's function) for holes is defined as

$$G(k;t_c,t_c') = -i\langle T_C\{h_k(t_c)h_k^\dagger(t_c')\}\rangle, \tag{10}$$

which can be rewritten for the initial state introduced above as

$$G(k;t_c,t_c') = -i\sum_{k_i} f(k_i)^2\langle 0| \times T_C\left\{U_C h_{k_i}(0_c^<)h_k(t_c)h_k^\dagger(t_c')h_{k_i}^\dagger(0_c^>)\right\}|0\rangle. \tag{11}$$

The real-time Green's functions are introduced by

$$G_{ij}(k;t,t') = G(k;t^{a_i},t'^{a_j}), \tag{12}$$

where a_1 and a_2 take $>$ and $<$. Here, G_{11} and G_{22} are the causal and anticausal Green's functions, respectively, and G_{12} and G_{21} are the lesser and greater Green's functions, characterizing the particle distribution, respectively. From these components, the retarded Green's function is given by

$$\begin{aligned} G^R(k;t,t') &= G_{11}(k;t,t') - G_{12}(k;t,t') \\ &= G_{21}(k;t,t') - G_{22}(k;t,t'). \end{aligned} \tag{13}$$

The one-particle excitation spectra for holes are defined by

$$A(k;\omega,t') = -\frac{1}{\pi}\mathrm{Im}[G^R(k;\omega,t')], \tag{14}$$

where we define the Fourier transform of the real-time Green's function given by

$$G(\omega,t') = \int d(t-t')e^{i\omega(t-t')}G(t-t',t'). \tag{15}$$

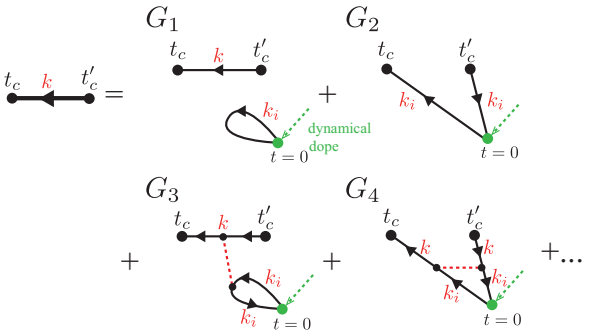

FIG. 3. (Color online) Feynman diagrams for one-particle Green's functions. Solid and dashed lines represent the hole Green's functions, $g(k;t)$, and the magnon Green's functions, $d(k;t)$, respectively, defined in the vacuum state.

In addition, we introduce one-particle Green's functions defined as expectations with respect to the vacuum state $|0\rangle$ as

$$g(k;t_c,t_c') = -i\langle 0|T_C\{U_C h_k(t_c)h_k^\dagger(t_c')\}|0\rangle \tag{16}$$

for a hole and

$$d(q;t_c,t_c') = -i\langle 0|T_C\{U_C \alpha_q(t_c)\alpha_q^\dagger(t_c')\}|0\rangle \tag{17}$$

for a magnon. The real-time Green's functions, $g(k;t-t')$ and $d(q;t-t')$, are obtained by projections onto the real-time axis and depend only on the time difference $t-t'$. The lesser component $g_{12}(k;t,t') = 0$, because there are no holes in the vacuum state. We show later that $G(t_c,t_c')$ in Eq. (10) is given by combinations of $g(k;t_c,t_c')$ and $d(k;t_c,t_c')$, and $g(k;t_c,t_c')$ is calculated by using the SCB approximation explained in Sec. III D.

The Green's function $G(t_c,t_c')$ in Eq. (10) is a four-point function, i.e., includes four fermion operators. The perturbation expansion with respect to M_{kq} is adopted to evaluate the Green's function. This is a reasonable approximation in the weak photodoped case where dynamically doped holes are dilute and do not frequently come across holes injected by probe photon. Figure 3 shows the Feynman diagrams in a series expansion up to the second order of M_{kq}. The zeroth-order terms, G_1 and G_2, are represented by products of $g(t_c,t_c')$ as $G_1 \sim -ig(t_c,t_c')g(0_c^<,0_c^>)$ and $G_2 \sim ig(t_c,0_c^>)g(0_c^<,t_c')$. In the second-order terms, G_3 and G_4, the two Green's functions are connected by the magnon Green's function. Diagrams for G_1 and G_3 represent "direct" processes, and G_2 and G_4 represent "exchange" processes where a dynamically doped hole is exchanged with an additionally introduced hole. The real-time Green's functions are obtained from the nonequilibrium Green's function on the Keldysh contour by the standard analytical continuation. Details are given in, for example, Refs. [29–31]. Here we exhibit an example; G_3 defined on the Keldysh contour is given by

$$\begin{aligned} G_3(k;t_c,t_c') = -\sum_{k_i} f(k_i)^2 \frac{z^2 M_{k0}M_{k_i0}}{2} \int_C dt_{2,c}\int_C dt_{3,c} g(k;t_c-t_{2,c})g(k;t_{2,c}-t_c')g(k_i;0_c'-t_{3,c})g(k_i;t_{3,c}-0_c') \\ \times (d(0;t_{2,c}-t_{3,c}) + d(0;t_{3,c}-t_{2,c})). \end{aligned} \tag{18}$$

The real-time Green's function is obtained by projecting the contour times t_c, t'_c, $t_{2,c}$, $t_{3,c}$ onto the real times and by introducing Keldysh indices. We have the explicit form

$$G_{3,ij}(k;t,t') = -\sum_{k_i} f(k_i)^2 \frac{z^2 M_{k0} M_{k_i 0}}{2} \int_{t'}^{t} dt_2 \int_{t'}^{t} dt_3 \sum_{\alpha,\beta,i',j',i'',j''=1,2} \delta_{i'j'} \tau^z_{j'\alpha} \delta_{i''j''} \tau^z_{i''\beta} g_{ii'}(k;t-t_2) g_{j'j}(k;t_2-t') \times g_{2i''}(k_i;-t_3) g_{j''1}(k_i;t_3)(d_{\alpha\beta}(0;t_2-t_3)+d_{\beta\alpha}(0;t_3-t_2)), \tag{19}$$

where τ^z is the z component of the Pauli matrix. By summing up the Keldysh indices and using a relation in Eq. (13), we obtain the retarded component $G^R_{3,ij}(k;t,t')$.

Explicit forms of the retarded components are given as

$$G^R_1(k;t,t') = g^R(k;t-t'), \tag{20}$$

$$G^R_2(k;t,t') = 0, \tag{21}$$

$$G^R_3(k;t,t') = \sum_{k_i} f(k_i)^2 \frac{z^2 M_{k0} M_{k_i 0}}{2} \int_{t'}^{t} dt_2 \int_{0}^{t_2} dt_3 g^R(k;t-t_2) g^R(k;t_2-t') |g^R(k_i;t_3)|^2 (d^R(0;t_2-t_3)+d^{R*}(0;t_2-t_3)), \tag{22}$$

$$G^R_4(k;t,t') = \sum_{k_i} f(k_i)^2 \frac{(-z^2)}{2} \int_{t'}^{t} dt_2 \int_{t'}^{t_2} dt_3 g^R(k;t-t_2) g^R(k_i;t_2) g^{R*}(k_i;t_3) g^R(k;t_3-t') \times \left(M^2_{k,k-k_i} d^R(k-k_i;t_2-t_3) + M^2_{k_i,k_i-k} d^{R*}(k_i-k;t_2-t_3) \right). \tag{23}$$

As shown in Eq. (20), G_1 does not depend on the initial state and is simply a one-particle Green's function in a Mott insulator, since additional doped holes do not interact with a dynamically doped hole. We have $G^R_2 = 0$, because G_2 includes the so-called electron line, $g(0,t' > 0)$, which vanishes in the t-J model at half-filling. The remaining terms, G_3 and G_4, explicitly depend on double times, t and t', and characterize the transient processes.

C. Optical conductivity

To calculate the optical conductivity in a transient state, we set up the Hamiltonian $\mathcal{H}(\boldsymbol{A})$, where the electric field is introduced as a Peierls phase in the t term of the Hamiltonian defined in Eq. (3). The current operator is given as

$$\boldsymbol{j} = -c \frac{\partial \mathcal{H}(\boldsymbol{A})}{\partial \boldsymbol{A}} = -\frac{iet_0}{\hbar} \sum_{\langle ij \rangle} \boldsymbol{\delta}_{ij} (a^\dagger_j h^\dagger_i h_j - h^\dagger_j h_i a_j), \tag{24}$$

where $\boldsymbol{A}$ is a vector potential and $\boldsymbol{\delta}_{ij}$ is a vector connecting nearest-neighbor sites i and j. Here, we take $e = 1$, $c = 1$, and $\hbar = 1$, for simplicity. By applying the Bogoliubov and Fourier transformations, the current operator can be rewritten as

$$\boldsymbol{j} = -\frac{1}{\sqrt{N}} \sum_{kq} \boldsymbol{V}_{kq} j_{kq}, \tag{25}$$

where we define

$$j_{kq} = \alpha^\dagger_q h^\dagger_{k-q} h_k + h^\dagger_k h_{k-q} \alpha_q \tag{26}$$

and

$$\boldsymbol{V}_{kq} = u_q \boldsymbol{v}_{k-q} + v_q \boldsymbol{v}_k, \tag{27}$$

with $\boldsymbol{v}_k = \partial \epsilon_k / \partial k$ and $\epsilon_k = -(zt_0/2)(\cos ak_x + \cos ak_y)$.

The optical conductivity is formulated within a linear response regime for an electric field $\boldsymbol{E}(t) = \boldsymbol{E} e^{-i\nu t}$ for probe photons, where ν is the photon frequency. Optical conductivity is defined as the response function for an electric current $\mathcal{J}(t) \equiv \langle \boldsymbol{j}(t) \rangle$ at time t induced by an electric field $\boldsymbol{E}(t')$ at time t'. This is given as

$$\left. \frac{\partial \mathcal{J}_\alpha(t)}{\partial E_\beta} \right|_{E=0} = \int_{-\infty}^{t} dt' \sigma^{(\nu)}_{\alpha\beta}(t,t') e^{-i\nu t'}, \tag{28}$$

where $E_\beta = [\boldsymbol{E}]_\beta$. From Eq. (25), the left-hand side is divided into two parts as

$$\frac{\partial \mathcal{J}_\alpha(t)}{\partial E_\beta} = -\frac{1}{\sqrt{N}} \sum_{kq} \left(\frac{\partial V^\alpha_{kq}}{\partial E_\beta} \langle j_{kq}(t) \rangle + V^\alpha_{kq} \frac{\partial}{\partial E_\beta} \langle j_{kq}(t) \rangle \right), \tag{29}$$

where $V^\alpha_{kq} = [\boldsymbol{V}_{kq}]_\alpha$. This is calculated from Eqs. (26) and (27); the optical conductivity can then be explicitly given as

$$\sigma^{(\nu)}_{\alpha\beta}(t,t') = -\frac{1}{\nu} \{ \delta(t-t') i \langle \mathcal{E}^{\alpha\beta}(t) \rangle + \theta(t-t') \langle [j_\alpha(t), j_\beta(t')] \rangle \}, \tag{30}$$

where $\mathcal{E}^{\alpha\beta}$ is the energy stress tensor defined by

$$\mathcal{E}^{\alpha\beta} = \frac{zt}{\sqrt{N}} \sum_{kq} \widetilde{M}^{\alpha\beta}_{kq} (h^\dagger_k h_{k-q} \alpha_q + \alpha^\dagger_q h^\dagger_{k-q} h_k), \tag{31}$$

and

$$\widetilde{M}^{\alpha\beta}_{kq} = \delta_{\alpha\beta} \left(u_q \widetilde{\gamma}^\alpha_{k-q} + v_q \widetilde{\gamma}^\alpha_k \right), \tag{32}$$

with $\widetilde{\gamma}^\alpha_k = (\cos k_\alpha)/2$. The first and second terms in Eq. (30) represent the diamagnetic and paramagnetic components, respectively. We assume no electric current before applying

the electric field. The paramagnetic component is given in the Keldysh formalism by

$$\langle [j_\alpha(t), j_\beta(t')] \rangle = \sum_{a=<,>} (\delta_{a,<} - \delta_{a,>}) \langle j_\alpha(t_c^<) j_\beta(t_c'^a) \rangle. \quad (33)$$

For convenience, we introduce the current-current response function as

$$\chi_{\alpha\beta}(t,t') = -i\theta(t-t')\langle [j_\alpha(t), j_\beta(t')] \rangle. \quad (34)$$

We define the optical conductivity spectra at time t by introducing the Fourier transformation as

$$\sigma_{\alpha\beta}(\omega,t) = \int_{-\infty}^{\infty} d(t-t') e^{i\omega(t-t')} \sigma_{\alpha\beta}^{(\nu)}(t,t'). \quad (35)$$

This has a physical meaning only at $\omega = \nu$, because

$$\begin{aligned} \mathcal{J}_\alpha(t) &= \int_{-\infty}^{t} dt' \sigma_{\alpha\beta}^{(\nu)}(t,t') E_\beta e^{-i\nu t'} \\ &= \sigma_{\alpha\beta}^{(\nu)}(\omega = \nu, t) E_\beta(t), \end{aligned} \quad (36)$$

where the relation $\sigma_{\alpha\beta}^{(\nu)}(t,t') = 0$ for $t - t' < 0$ is used. The real part of the optical conductivity is given by

$$\mathrm{Re}\sigma(\omega,t) = \pi\delta(\omega) D_{\alpha\beta}(t) - \frac{\omega}{\omega^2 + \eta^2} \mathrm{Im}\chi_{\alpha\beta}(\omega,t), \quad (37)$$

with an infinitesimal positive constant η. The first term is the Drude component, which can be divided into two parts as

$$D_{\alpha\beta}(t) = D_{\alpha\beta}^{\mathrm{dia}}(t) + D_{\alpha\beta}^{\mathrm{para}}(t), \quad (38)$$

with the diamagnetic component given by

$$D_{\alpha\beta}^{\mathrm{dia}}(t) = -\langle \mathcal{E}^{\alpha\beta}(t) \rangle, \quad (39)$$

and the paramagnetic one by

$$D_{\alpha\beta}^{\mathrm{para}}(t) = \mathrm{Re}\chi_{\alpha\beta}(\omega = 0, t). \quad (40)$$

We calculate the optical conductivity by the perturbation expansions. Within the lowest-order term, the diamagnetic and paramagnetic components are given by

$$D_{\alpha\beta}^{\mathrm{dia}}(t) = \frac{2}{N} \sum_{k_i,q} f(k_i)^2 \int dt_2 \tilde{M}_{k_i,q}^{\alpha\beta} M_{k_i,q} h_{k_i,q}(t,t_2) \quad (41)$$

and

$$\chi_{\alpha\beta}(t,t') = -\frac{2}{N} \sum_{k_i,q} f(k_i)^2 V_{k_i,q}^{\alpha} V_{k_i,q}^{\beta} h_q(t,t'), \quad (42)$$

respectively. Here we define

$$\begin{aligned} h_{k_i,q}(t,t') = \mathrm{Im}[&g^{R*}(k_i;t) g^R(k_i - q; t - t') \\ &\times g^R(k_i,t') d^R(q; t - t')]. \end{aligned} \quad (43)$$

These two contributions are diagrammatically expressed by Fig. 4.

It is worth noting that there is an uncertainly relation between t and ω in the function $\mathrm{Re}\sigma(\omega,t)$ introduced in Eq. (35), where the linear response theory and the Fourier transformation are utilized. Only for $\omega \geqslant t^{-1}$ is this function $\mathrm{Re}\sigma(\omega,t)$ recognized as a response function for the external field with frequency ω. A numerical test for validity of $\mathrm{Re}\sigma(\omega,t)$ based on the linear-response theory is given in Ref. [22]. In the pump-probe experiments on real materials, there are several contributions to the damping factors in $\sigma(\omega,t)$, such as impurities and vacancies, which are not taken into account in the present formalism. These extrinsic factors change the δ function for the Drude peak into a Lorentzian peak $\Gamma/(\omega^2 + \Gamma^2)$, which is relevant as a response function for a condition of $t \geqslant 1/\Gamma$.

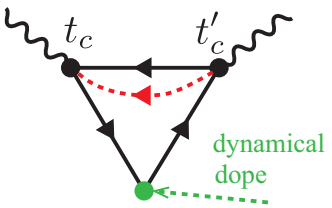

FIG. 4. (Color online) Feynman diagram for the optical conductivity. Solid and dashed lines represent the hole Green's function, $g(k;t)$, and the magnon Green's function, $d(q;t)$, respectively, defined in the vacuum state; wavy lines represent the light.

D. Self-consistent Born approximation

As shown in Eqs. (20)–(23) and (41)–(43), the full Green's functions and the optical conductivity are represented by $g^R(k;t)$. We evaluate $g^R(k;t)$ by using the SCB approximation, which is known to describe well chemically doped hole dynamics in AFLRO, in particular, for $\alpha \sim 1$. [32,33]

We iteratively solve the Dyson's equation given by

$$g^{R^{-1}}(k;\omega) = g^{R(0)^{-1}}(\omega) - \Sigma^R(k;\omega), \quad (44)$$

where the self-energy is given by

$$\Sigma^R(k;\omega) = i\frac{z^2 t^2}{N} \sum_q \int \frac{d\omega'}{2\pi} M_{kq}^2 g^R(k-q; \omega - \omega') d^R(q;\omega'), \quad (45)$$

which is diagrammatically shown in Fig. 5. The bare hole Green's function is given by

$$g^{R(0)}(\omega) = \frac{1}{\omega + i\eta}. \quad (46)$$

For the magnon Green's function, for simplicity, it is replaced by the bare magnon Green's function,

$$d^R(q;\omega) = \frac{1}{\omega - \omega_q + i\eta}. \quad (47)$$

Although the magnon Green's function can be estimated by a series expansion, the lowest-order self-energy of the bubble

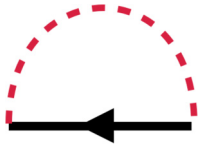

FIG. 5. (Color online) Self-energy of a hole Green's function in the self-consistent Born approximation. Solid and dashed lines represent the hole Green's function, $g(k;t)$, and the magnon Green's function, $d(k;t)$, respectively, defined in the vacuum state.

type vanishes, since the so-called electron line, where the electron creation operator acts on a vacuum, disappears in the t-J model.

IV. NUMERICAL RESULTS

In the numerical calculations, we adopt two-dimensional square lattices with $N \times N$ sites, where N is taken to be 32 in most of the calculations (and 128 in Fig. 6). A typical mesh number for energy is 512. We assume, for simplicity, that the momentum in the dynamically doped hole has a specific value k_0, i.e., $f(k_i) = \delta_{k_i k_0}\sqrt{\delta_d}$ in Eq. (6), where holes with momentum k_i of density δ_d are independently injected into the system and do not interact with each other. We take $\delta_d = 0.01$, which is realistic as a photodoped carrier density in optical pump-probe experiments [27,28]. All energies and times in the numerical calculations are measured by t_0 and t_0^{-1}, respectively. We adopt the first Brillouin zone for the original square lattice—not the reduced one for the Néel state. We show numerical results in a wide parameter range of the anisotropic parameter $\alpha = J_\perp/J_\parallel$. In particular, we adopt $\alpha = 0.2$ and 0.8 as prototypical parameter values for the Ising-like and Heisenberg-like cases, respectively, instead of $\alpha = 0$ and 1. This is because at $\alpha = 0$, the transient carrier dynamics is totally determined by the dispersionless magnons, and broad incoherent spectral weights at $\alpha = 1$ cause difficulty in data analyses introduced later.

A. Electronic state before dynamical doping

Before showing the transient electronic state, we first show results for one-particle excitation spectra before dynamical doping. The present results are consistent with those published in Refs. [32] and [33]. Figure 6 shows contour maps of the one-particle excitation spectra given by

$$a(k;\omega) = -\frac{1}{\pi}\mathrm{Im}\, g^R(k;\omega) \tag{48}$$

in the k-ω plane. We chose the anisotropy parameter as $\alpha(\equiv J_\perp/J_\parallel) = 0.8$ and 0.2 in Figs. 6(a) and 6(b), respectively. Ladder-like multiple-peak structures are seen in the Ising-like case [Fig. 6(b)], where low-lying peaks are separated by $J^{2/3}$, as reported in Ref. [32]. In the case of large α, an incoherent background and dispersive character owing to spin fluctuation are seen. The lowest dispersive branch, centered at $\omega \simeq -2$, is the QP band, where weak dispersion is seen along the $(\pi,0)$-$(\pi/2,\pi/2)$ line, and a shallow minimum appears at $(\pi/2,\pi/2)$; i.e., small hole pockets appear around $(\pi/2,\pi/2)$. The large QP dispersion in Fig. 6(a) implies that carrier propagation in an AFLRO background is caused by spin fluctuation.

Figure 7 shows α dependencies of the imaginary parts of the self-energy at the QP peak for several values of J, i.e., $-\mathrm{Im}\Sigma(k;\omega_k^{\mathrm{QP}}) + \eta$, where ω_k^{QP} is the QP band energy at momentum k. Results at $k = (\pi/2,\pi/2)$ and $k = (0,0)$ are shown in Figs. 7(a) and 7(b), respectively. Different α

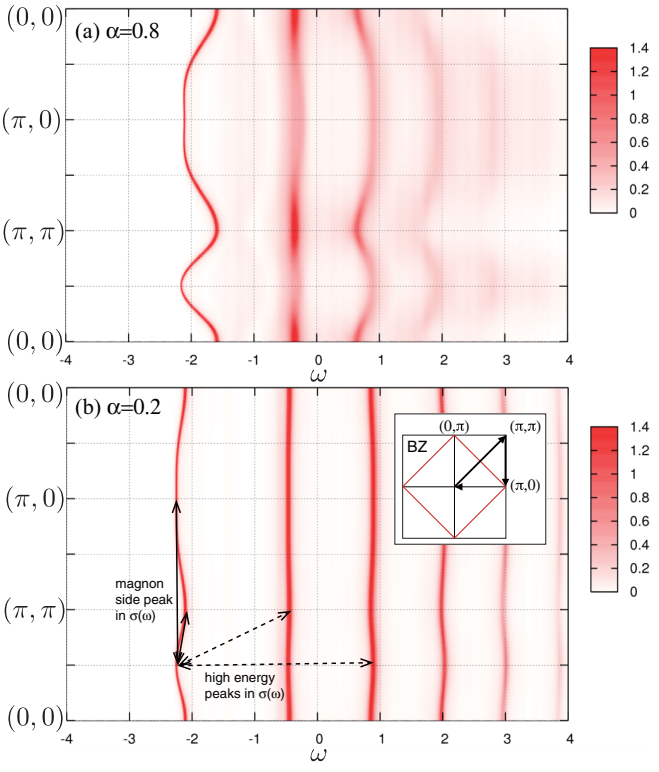

FIG. 6. (Color online) One-particle excitation spectra before dynamical doping, $a(k;\omega) = -(1/\pi)\mathrm{Im}g^R(k;\omega)$. Parameters are chosen to be $N = 128$, $J = 0.4$, and damping constant $\eta = 0.01$. The anisotropy parameter is $\alpha = 0.8$ (a) and $\alpha = 0.2$ (b). Arrows in (b) represent examples of transitions characterizing peaks in optical conductivity in transient states (see Sec. IV C).

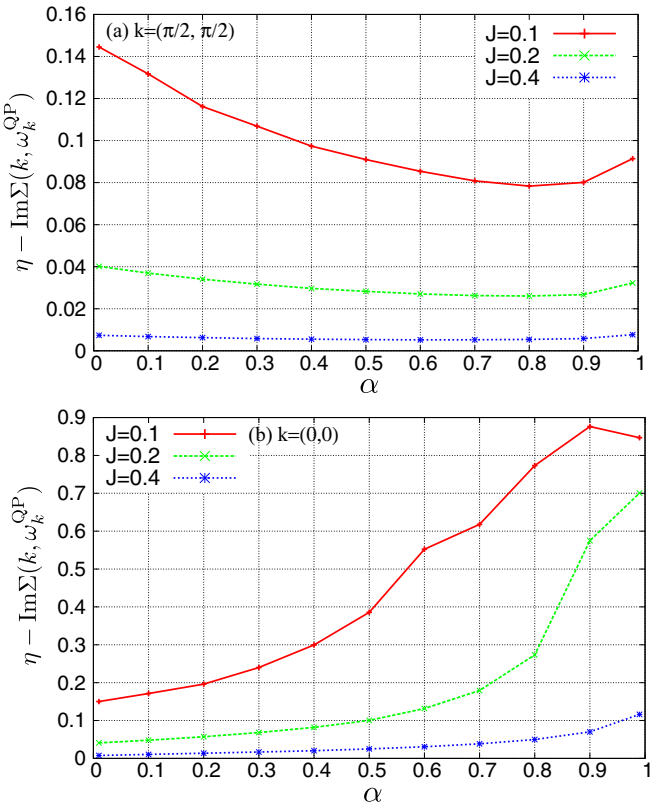

FIG. 7. (Color online) Imaginary parts of the self-energy at the QP band for several J, $-\mathrm{Im}\Sigma(k,\omega_k^{\mathrm{QP}}) + \eta$, where ω_k^{QP} is the QP band energy at momentum k. The momentum as a parameter in the Green's function is chosen to be (a) $k = (\pi/2,\pi/2)$ and (b) $k = (0,0)$.

dependencies are seen in the cases of $k = (\pi/2,\pi/2)$ and $k = (0,0)$; $-\mathrm{Im}\Sigma(k;\omega_k^{\mathrm{QP}})$ decreases (increases) with increasing α at $k = (\pi/2,\pi/2)$ [$k = (0,0)$], except in the vicinity of $\alpha = 1$. This opposite behavior implies that the coherent QP motion at $k = (\pi/2,\pi/2)$ is promoted by quantum spin fluctuations and that the higher-energy carriers at $k = (0,0)$ are incoherently scattered by spin fluctuations.

B. One-particle excitation in transient states

In this subsection, numerical results of the one-particle excitation spectra in the transient state are presented. As shown in Sec. III B, the one-particle retarded Green's function is given in the perturbation expansion as $G^R(k;t,t') = \sum_{i=1}^{4} G_i^R(k;t,t')$, where $G_1^R(k;t,t') = g^R(k;t,t')$, which is the retarded Green's function without dynamical doping, and $G_2^R(k;t,t') = 0$. Then we define the difference between $G(k;\omega,t')$ and $g^R(k;\omega)$ as

$$\delta G^R(k;\omega,t') \equiv G^R(k;\omega,t') - g^R(k;\omega) = G_3^R(k;\omega,t') + G_4^R(k;\omega,t'), \quad (49)$$

and the corresponding spectral weight as

$$\delta A(k;\omega,t') = -\frac{1}{\pi}\mathrm{Im}\delta G^R(k;\omega,t'), \quad (50)$$

where the sum rule

$$\int_{-\infty}^{\infty} \delta A(k;\omega,t')d\omega = 0 \quad (51)$$

exists for any t'. We have checked that Eq. (51) is satisfied in the numerical calculations within numerical errors.

For the momentum k as a parameter of the one-particle Green's function and the momentum k_0 of the dynamically doped hole, we have some rules: that $G_3 = 0$ when both k and k_0 are on the X-M line and that $G_4 = 0$ when either k or k_0 is on this line. By taking into account these facts and the QP dispersion, we consider the following three cases in the numerical calculations:

(A) $k = (0,0)$, $k_0 = (0,0)$,
(B) $k = (0,0)$, $k_0 = (\pi/2,\pi/2)$, and
(C) $k = (\pi/2,\pi/2)$, $k_0 = (0,0)$.

Let us begin with case A. Figure 8(a) shows the time dependencies of $\delta A(\omega;t')$ in case A [$k = (0,0)$, $k_0 = (0,0)$]. The parameter values are chosen to be $J = 0.4$ and $\alpha = 0.8$. With increasing elapsed time t' after dynamical doping, remarkable changes appear around $\omega \simeq -1.6$, -0.5, and 0.4, which correspond to the lowest three peak energies in $\mathrm{Im}g^R(k,\omega)$ before dynamical doping [see Fig. 6(a)]. That is, the main three peaks shift to the lower-energy side. In addition, small peaks, indicated by black arrows in Fig. 8(a), show oscillatory behaviors with time evolution. To examine the origin of these transient changes in more detail, the calculated one-particle excitation spectra, as well as the optical conductivity spectra, are analyzed by using the DPA introduced in Ref. [32], where peaks in $\mathrm{Im}g^R(k;\omega)$ and $\mathrm{Im}d^R(k;\omega)$ are represented by a series of Lorentz functions. Details are presented in the Appendix. As shown in Eq. (A3), $\delta G^R(\omega,t')$ has poles at $\epsilon_k^i \pm \omega_{q=0}$, in addition to ϵ_k^i originating from $\mathrm{Im}g^R(k;\omega)$. These newly appearing peaks, located around the sum of the original QP band energy and the magnon energy ω_q, are termed "magnon side peaks."

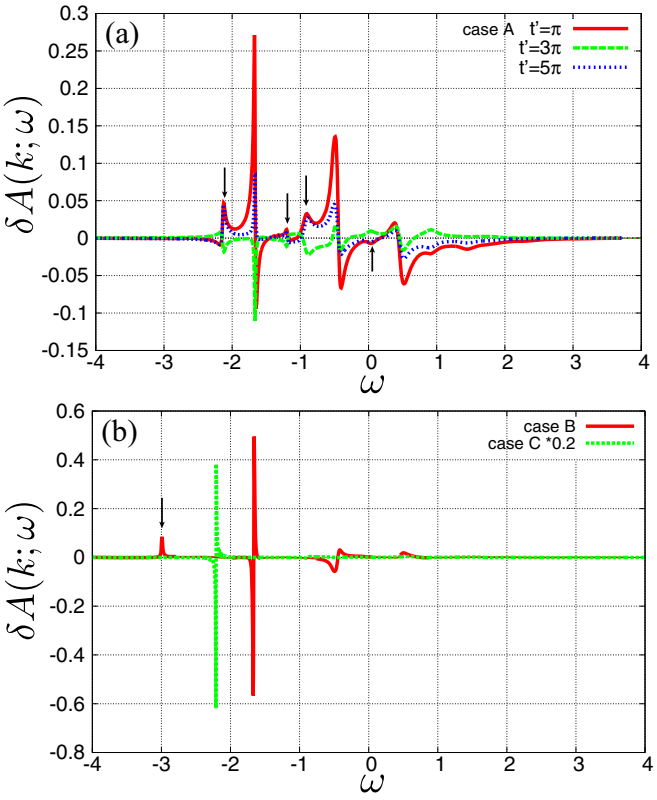

FIG. 8. (Color online) Time dependencies of changes in the one-particle excitation spectra, $\delta A(k;\omega)$. We chose $t' = \pi$, 3π, and 5π. (a) Results in case A [$k = (0,0)$, $k_0 = (0,0)$]. Black arrows indicate "magnon side peaks" (see the text). (b) Results in case B [$k = (0,0)$, $k_0 = (\pi/2,\pi/2)$] and case C [$k = (\pi/2,\pi/2)$, $k_0 = (0,0)$]. Results in case C are multiplied by 0.2. The black arrow indicates the "exchange peak" (see the text). Other parameters are chosen to be $N = 32$, $J = 0.4$, $\alpha = 0.8$, and $\eta = 0.01$.

To examine the oscillatory behaviors shown above, we calculate the integrated spectral weight change given by

$$B(k;t') = \int_{-\infty}^{0} \delta A(k;\omega,t')d\omega. \quad (52)$$

Results in case A for several values of the anisotropy parameter α are given in Fig. 9(a). Oscillations in $B(k;t')$ are clearly shown in the cases of large α, and the time period decreases with decreasing α. From the DPA analyses, one finds that the oscillations are characterized by $T_{sb} \equiv 2\pi/\omega_{q=0} \propto 1/(J\sqrt{1-\alpha^2})$ [see the exponential factor in Eq. (A3)]. For large α, $B(k;t')$ has almost a single-frequency component with T_{sb}^{-1}. This implies that the oscillating behavior originates almost solely from the magnon side peaks [indicated by arrows in Fig. 8(a)]. In contrast, multifrequency oscillatory behavior for small α is attributed to the fact that other peaks make relevant contributions to $\delta A(k;t')$. One of the dominant contributions originates from peaks at $\omega = (\epsilon^b - \epsilon^c + \epsilon^d) - i(\Gamma^b + \Gamma^c + \Gamma^d)$ in Eq. (A3). These represent transitions between the inter-ladder-type bands and are termed "exchange peaks."

Next, we show the results in other cases of momenta k and k_0. Results for $\delta A(k;\omega,t')$ and $B(k;t')$ are given in

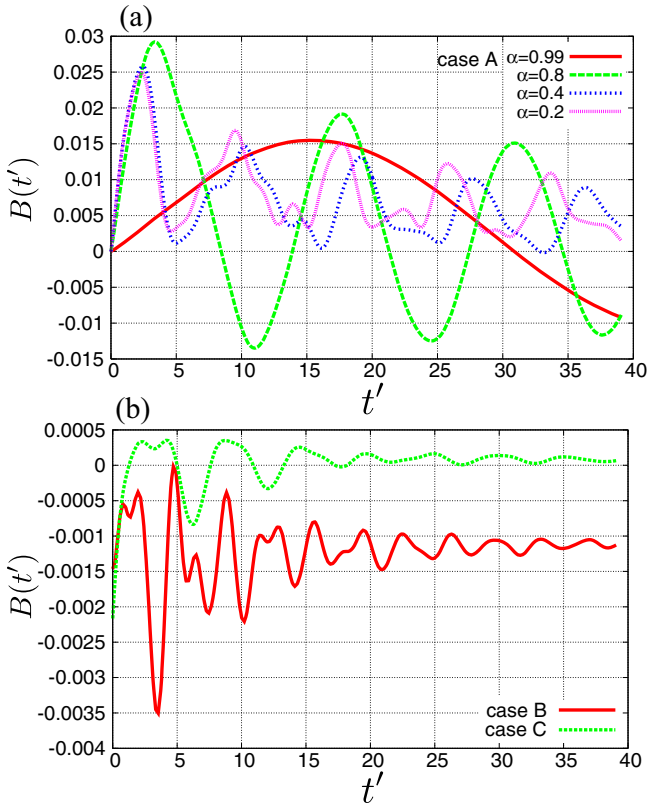

FIG. 9. (Color online) Time dependencies of the integrated spectral weight $B(t)$ defined in Eq. (52). (a) Results in case A [$k = (0,0)$, $k_0 = (0,0)$]. The anisotropy parameter is chosen to be $\alpha = 0.99$, 0.8, 0.4, and 0.2. (b) Results in case B [$k = (0,0)$, $k_0 = (\pi/2,\pi/2)$] and case C [$k = (\pi/2,\pi/2)$, $k_0 = (0,0)$]. Other parameter values are chosen to be $N = 32$, $J = 0.4$, $\alpha = 0.8$, and $\eta = 0.01$.

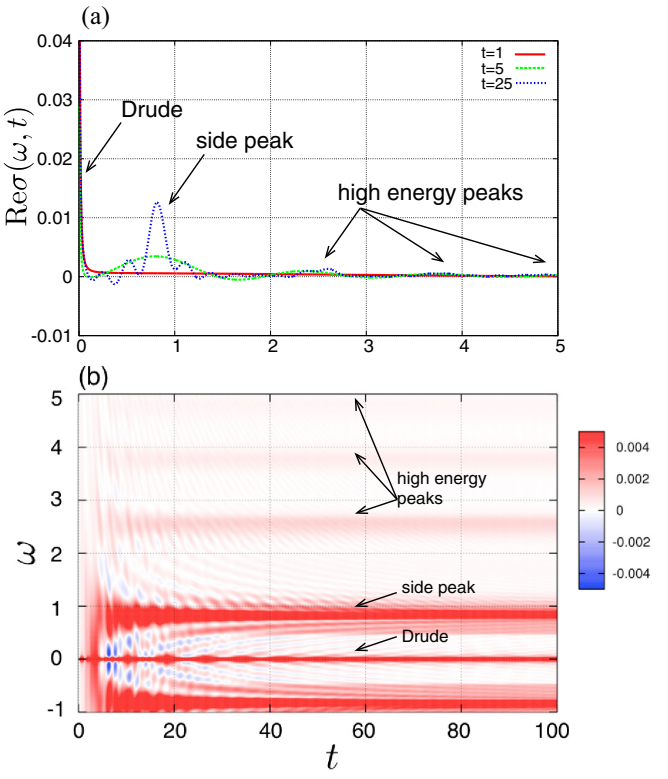

FIG. 10. (Color online) Transient optical conductivity spectra at several times; $t = 1$ (red line), 5 (green line), and 25 (blue line). The momentum of the dynamically doped hole is chosen to be $k_0 = (\pi/2,\pi/2)$. (b) Contour plot of optical conductivity spectra in the time-frequency plane. Other parameters are chosen to be $J = 0.4$ and $\alpha = 0.8$.

Fig. 8(b) and Fig. 9(b), respectively, in case B [$k = (0,0)$, $k_0 = (\pi/2,\pi/2)$] and case C [$k = (\pi/2,\pi/2)$, $k_0 = (0,0)$]. As shown in Fig. 8(b), in both case B and case C, dominant changes in $\delta A(k,\omega)$ are shown as shifts of the main peaks in $\mathrm{Im}g^R(k,\omega)$, and contributions from the magnon side peaks are small. In case B, a small peak appears around $\omega \simeq -3$ (indicated by the black arrow); this is below the lowest QP band before dynamical doping. Since a similar peak structure was observed in the previous calculations in the case with chemical doping [43], this is due to a carrier doping effect. For the results of $B(k;t')$ shown in Fig. 9(b), there are multifrequencies in oscillatory behaviors for both case B and case C, unlike case A with a large α. Damping of the oscillatory behavior is faster in case C than in case B. This is interpreted from the imaginary part of the self-energy before dynamical doping; that is, the damping rate $-\mathrm{Im}\Sigma(k;\omega_k^{\mathrm{QP}})$ at $k = (0,0)$ is higher than that at $k = (\pi/2,\pi/2)$ for any value of α, as shown in Fig. 7.

C. Optical conductivity in transient states

In this subsection, numerical results for the transient optical conductivity spectra after dynamical doping are presented. We note that there are no finite values in the optical conductivity spectra before dynamical hole doping in the t-J model. We focus on the (xx) component of the optical conductivity spectra.

First, we present results where the momentum of the dynamically doped hole is chosen to be $k_0 = (\pi/2,\pi/2)$, which corresponds to the lowest QP peak in $\mathrm{Im}g^R(k;\omega)$. In Fig. 10(a), the time dependencies of the real parts of the optical conductivity spectra are presented. Just after the dynamical hole doping at $t = 0$, only the Drude peak is confirmed at $t = 1$. After a lapse of time, subpeak structures appear and grow around $\omega = 0.8$, $\omega = 2.5$, and other energies. The peak at $\sim$0.8 is termed the "side peak," and other peaks, located around 2.5, 3.8, etc., are termed "high-energy peaks," henceforth. As explained later, the emergence of these peaks implies that the dynamically doped hole is dressed by magnons. From the DPA analyses, the Drude and finite-frequency peaks grow as t^2 and t^3, respectively, as shown in Eq. (A15).

A contour plot of $\sigma(\omega,t)$ in the ω-t plane is presented in Fig. 10(b). The time evolutions of the side peak and the high-energy peaks are clearly shown. The origins of the side peak and the high-energy peaks are clarified by using the DPA. In Eq. (A14), these peaks are characterized by poles of $h_{k_0,q}$, introduced in Eq. (43), at $\omega = \pm(\epsilon^b_{k_0-q} - \epsilon^c_{k_0} + \omega_q) + i(\Gamma^b_{k_0-q} - \Gamma^c_{k_0} + \eta)$, where ϵ^i_k and Γ^i_k are, respectively, the energy and a damping factor for the ith peak of $\mathrm{Im}g^R(k;\omega)$. The side peak and the high-energy peaks originate from poles with $b = c$ and $b \neq c$, respectively, and are attributed to the intraband transitions inside the lowest-energy QP band and the interband transitions between the ladder-like multiple bands,

respectively [see Fig. 6(a)]. Thus, the energies of the side peak and the high-energy peaks are mainly dominated by the band widths of the QP band and the energy differences between the ladder-like peaks, respectively. To clarify the role of magnons in the optical conductivity in more detail, we introduce a hypothetical situation in which the self-energy for the hole Green's function given in Eq. (45) is set to be 0 artificially. In this case, the QP band in $\mathrm{Im}g^R$ does not show dispersion, and magnons only appear in the current vertex. We observe that the high-energy peaks do not appear in the optical conductivity, and the energy of the side peak depends only on the magnon energy and amplitude of the current vertex. From these results, the time evolution of the optical conductivity is interpreted as the results of a dynamically doped hole being dressed by magnon clouds evolving in time.

The detailed time evolution for each peak is examined by introducing the integrated peak intensity around a peak position. This is defined by

$$I_i(t) = \int_{\omega_i-\delta_i}^{\omega_i+\delta_i} d\omega \mathrm{Re}\sigma(\omega,t), \tag{53}$$

where the peak is identified by an index i, ω_i is the peak position at $t = 100$, and δ_i is the width in the integrated energy region. Numerical values of δ_i are chosen to be the energy where the peak intensities are almost 0. We define $i = 0$ and 1 for the Drude peak and the side peak, respectively, and $i \geqslant 2$ for the high-energy peaks. The time dependencies of $I_i(t)$ are shown in Figs. 11(a), 11(b), and 11(c) for $i = 0$ (Drude peak), $i = 1$ (side peak), and $i = 2$ (high-energy peak), respectively. Strong oscillatory behaviors are seen in all peaks, in particular, rapid oscillations at small α. These are attributed to ladder-like multiple peaks in $\mathrm{Im}g^R(k,\omega)$ and are identified as "coherent magnon oscillations."

Deferent α dependencies of the intensity are seen in the Drude and other peaks; $I_0(t)$ [$I_1(t)$ and $I_2(t)$] decreases (increases) with increasing anisotropic parameter α. These different α dependencies are interpreted as follows. As shown in Eqs. (37)–(43) and Eq. (A14), the intensities of the side peak and the high-energy peaks are given by the imaginary parts of $h_{k_i,q}(t,t')$. Since poles are located at $\omega = \pm(\epsilon_{bc} + \omega_q)$ which give a relation between the magnon and the hole momenta, these intensities are sensitive to the maganon and hole band dispersions. On the other hand, the Drude peak is given by the real part of $h_{k_i,q}(t,t')$, which is related to the integrated $h_{k_i,q}(t,t')$ in terms of energy. Therefore, the Drude peak intensity is sensitive not to details of the hole and magnon dispersions but to the coupling constants M_{kq} [Eq. (4)] and V_{kq} [Eq. (27)], which directly depend on α.

Next, slow dynamics, without fast oscillatory behavior, is examined by integrating $I_i(t)$ with respect to time since dynamical doping as

$$W_i(t) = \frac{1}{t}\int_0^t dt' I_i(t'). \tag{54}$$

Figure 12 shows the results normalized by $W_i(t)$ at $t = 100$; i.e., $\widetilde{W}_i(t) = W_i(t)/W_i(100)$. The anisotropy parameter is chosen to be $\alpha = 0.01$ and 0.99 in Figs. 12(a) and 12(b), respectively. Each data set smoothly converges to 1 at large t. That is, the dynamically doped hole gradually changes into

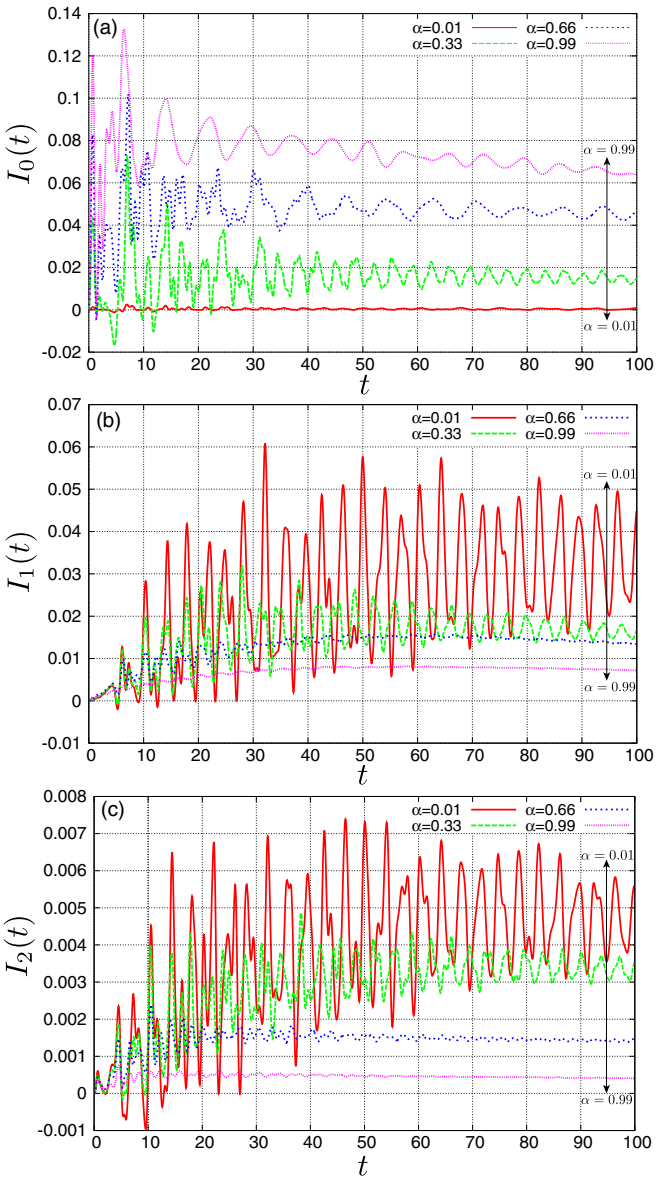

FIG. 11. (Color online) Time dependencies of the peak intensities $I_i(t)$ defined in Eq. (53) for several values of the anisotropy parameter α. (a) The Drude peak ($i = 0$), (b) the side peak ($i = 1$), and (c) the high-energy peak ($i = 2$). Parameters are chosen to be $k_0 = (\pi/2,\pi/2)$ and $J = 0.4$. Values for ω_i and δ_i in Eq. (53) are taken to be $(\omega_0,\delta_0,\omega_1,\delta_1,\omega_2,\delta_2) = (0,0.01,0.78,0.03,2.57,0.02)$ for $\alpha = 0.01$, $(0,0.01,0.81,0.07,2.60,0.05)$ for $\alpha = 0.33$, $(0,0.01,0.83,0.07,2.58,0.12)$ for $\alpha = 0.66$, and $(0,0.01,0.84,0.05,2.56,0.04)$ for $\alpha = 0.99$.

a quasisteady state with coherent oscillations. The relaxation times depend on the peaks and α; fast relaxations are seen in the Drude peak ($i = 0$) with $\alpha = 0.01$ and in the Drude and side peaks ($i = 0$ and 1) with $\alpha = 0.99$. We fit the time dependencies of $\widetilde{W}_i(t)$ by a simple exponential function $1 - \exp(-t/\tau)$, and we show relaxation times in Fig. 12(c). The α dependence is notable in the high-energy peak ($i = 2$ and 3); the relaxation is slow (fast) in the Ising-like (Heisenberg-like) case. As explained previously, the high-energy peak is attributed to the interband transition between the ladder-like multiple bands in

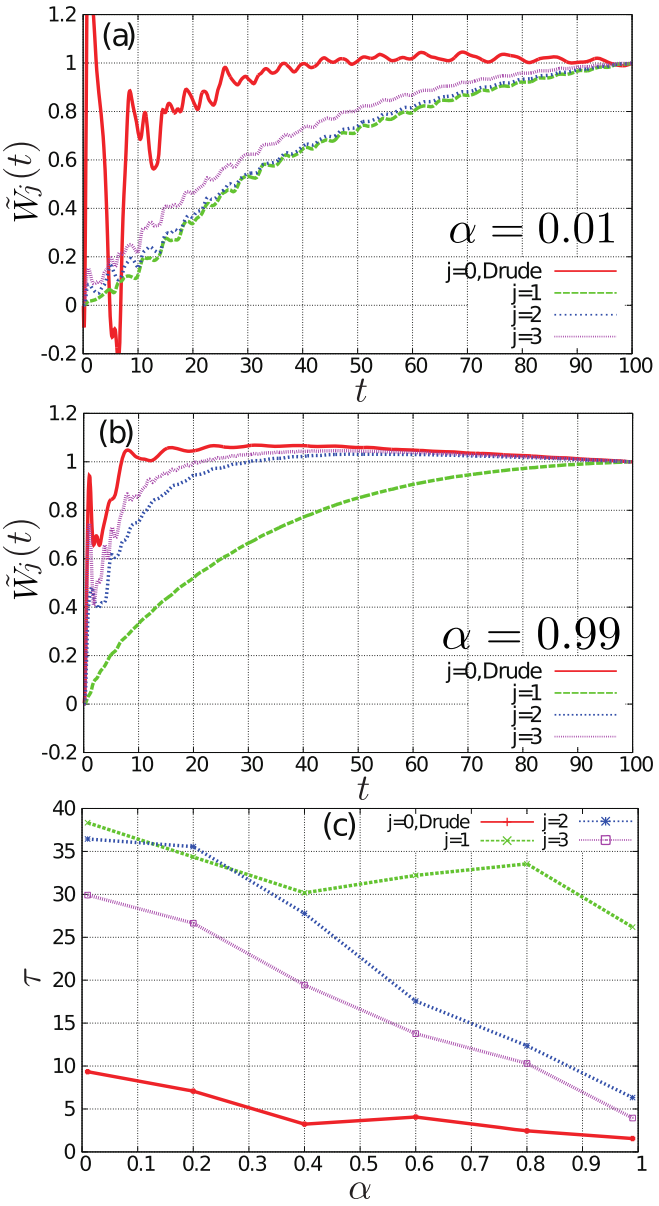

FIG. 12. (Color online) Time dependencies of $W_i(t)$ defined in Eq. (54) normalized at $t = 100$, i.e., $\widetilde{W}_i(t) = W_i(t)/W_i(100)$, for each peak. The anisotropy parameter is chosen to be $\alpha = 0.01$ (a) and 0.99 (b). (c) Relaxation time as functions of α for each peak. The parameter value is chosen to be $J = 0.4$.

Im$g^R(q,\omega)$. The scattering probability is high for the small energy difference between the bands for large α and low for the large energy difference between the bands for small α. The significant incoherent background in Img^R at large α induces additional transition pathways.

Finally, we show results for other momenta of dynamically doped holes. In Figs. 13(a) and 13(b), we present the optical conductivity spectra Re$\sigma(\omega,t)$ for $k_0 = (0,0)$ and $(\pi,0)$, respectively. In both cases, the Drude peak, the side peak, and the high-energy peaks are confirmed. The energy of the side peak for $k_0 = (0,0)$ is lower than those for $k_0 = (\pi/2,\pi/2)$ and $(\pi,0)$. This is explained by the DPA as the energy of the side peak being dominated by a pole at $\omega = \epsilon^b_{k_0-q} - \epsilon^c_{k_0} + \omega_q$

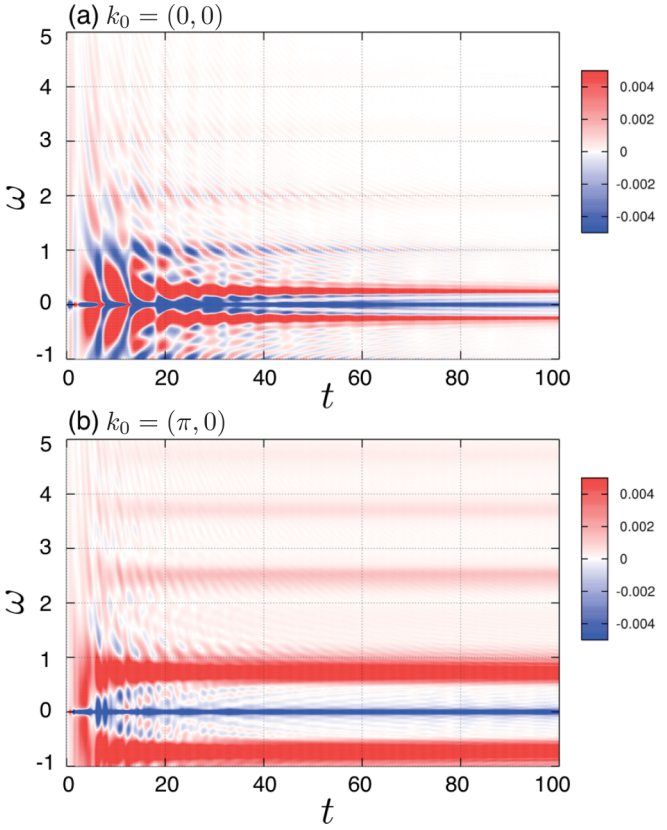

FIG. 13. (Color online) Contour plots of optical conductivity spectra in the cases of (a) $k_0 = (0,0)$ and (b) $k_0 = (\pi,0)$. Parameter values are chosen to be $J = 0.4$ and $\alpha = 0.8$.

with $b = c$, where $\epsilon^b_{k_0-q} - \epsilon^c_{k_0}$ is negative for any q in the case of $k_0 = (0,0)$. This k_0 dependence of the side peak energy is remarkable in large α, where the dispersions of magnons and holes are large.

Note that Fig. 13(b) looks similar to Fig. 10(b) for the side peak and the high-energy peak. This is because the QP band in Im$g^R(k,\omega)$ is nearly degenerate along $k = (\pi/2,\pi/2)$ and $(\pi,0)$. The most remarkable difference between Fig. 13(b) and Fig. 10(b) is seen in the sign of the Drude weight, which is negative in Fig. 13(b). The negative D, which is not realized in equilibrium states, represents the emission of photons in transient states. More detailed time profiles of D for several k_0 are presented in Fig. 14. Negative values for $k_0 = (\pi,0)$ and $(0,0)$ tend to be positive gradually. This negative value is interpreted as a population inversion and light emission. As shown in Fig 6(a), the second derivative of the QP band dispersion with respect to the momentum, $\partial^2\omega_k^{\rm QP}/\partial k^2$, is negative at $k = (\pi,0)$ and $(0,0)$ and positive at $k = (\pi/2,\pi/2)$. This convexity of the QP band in Im$g^R(k;\omega)$ for a dynamically doped hole determines the sign of D.

V. CONCLUSION

In conclusion, we have studied real-time hole dynamics injected into a Mott insulator with AFLRO. The transient optical conductivity spectra and one-particle excitation spectra are formulated by applying the Keldysh Green's function

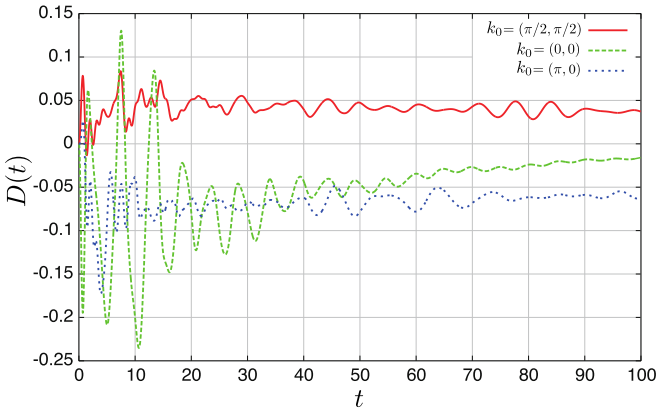

FIG. 14. (Color online) Time dependence of the Drude weight $D(t)$ for several momenta of the dynamically doped holes. Parameter values are chosen to be $J = 0.4$ and $\alpha = 0.8$. Solid, dashed, and dotted lines represent $k_0 = (\pi/2,\pi/2)$, $k = (0,0)$ and $k = (\pi,0)$, respectively.

formalism and the SCB approximation to the two-dimensional t-J model. Here we list the main results. In the early stage just after dynamical hole doping, only the Drude component appears, then the finite-energy incoherent components (termed the side peak and the higher-energy peaks) gradually grow [see Figs. 10(a) and 10(b)]. The side peak and higher-energy peaks are identified as the intra- and interband transitions of the ladder-type bands, respectively, associated with magnon excitations. In the small-t region, the intensities of the Drude and incoherent parts grow as t^2 and t^3, respectively. These time evolutions imply that a dynamically doped bare hole is gradually dressed by magnon clouds and changes into a spin polaron QP state. The time profiles of the Drude and incoherent peaks exhibit fast oscillatory components, i.e., coherent magnon oscillation, and slow relaxation dynamics scaled by an exponential function (see Fig. 11). The fast component is apparent in the small-α ($\equiv J_\perp/J_\parallel$) case (Ising-like case), where the magnon dispersion is almost flat and provides a single time scale. For the slow relaxation dynamics, only the higher-energy peaks show a strong α dependence [see Fig. 12(c)]. This is interpreted from the fact that the interband hole transitions by magnons are effective in the large-α case (Heisenberg-like case) where the magnon band width is large.

The present numerical calculations simulate the early stage in time-resolved pump-probe experiments. When we take $t = 0.5$ eV, the time scale $t = 30$ in the present calculation corresponds to about 40 fs, which is a realistic time scale in recent ultrafast optical experiments. Our calculations predict a time lag for observation of the incoherent component of the optical conductivity spectra associated with coherent magnon oscillation. Purely electronic processes of dynamically doped carriers are detected in careful measurements and analyses of the early stage of time-resolved optical spectra, where the dynamics of electron and hole carriers can be separated [23]. More direct tests of the present simulations will be performed by the photocarrier injection into the heterostructure where holes or electrons are selectively introduced into a sample [25–28].

It is worth mentioning that the present formalism is also applicable to real-time carrier dynamics doped into Mott insulators with an orbital degree of freedom. There are numerous studies of photoirradiation effects in orbitally degenerate correlated electron systems [34–38]. A doped Mott insulator with an orbital degree of freedom is described by the t-J type model [39,40], where a similar decomposition of the restricted hole operator [see Eqs. (3) and (5)] is introduced; doped carrier dynamics can be represented by a spin- and orbital-less fermion that interacts with the magnon and the "orbiton." One of the qualitative differences between an orbitally degenerate Mott insulator and the present single-band Mott insulator in this scheme is the fact that the occupied electron number in a specific orbital is not conserved [40]. This fact brings about a free kinetic term for fermions, $\mathcal{H}_t \sim \sum_k h_k^\dagger h_k$, where orbiton operators do not appear, in contrast to Eq. (3). Coupling between spin and orbital degrees of freedom [40,41] and static and dynamical Jahn-Teller effects [42] also provide qualitatively different real-time carrier dynamics from the present case of a Mott insulator with AFLRO.

ACKNOWLEDGMENTS

The authors thank H. Okamoto, S. Koshihara, and S. Iwai for helpful discussions. Parts of the numerical calculations were performed on the supercomputing systems at ISSP, the University of Tokyo. This work was supported by the Core Research Evolutional and Science and Technology program of the JST, the KAKENHI program of MEXT, and the Tohoku University "Evolution" program.

APPENDIX: DOMINANT POLE APPROXIMATION

In this Appendix, we present formalisms and results of the DPA introduced in Ref. [32] and utilized in Sec. IV. As shown in the results in Ref. [32], Ref. [33], and Fig. 6, the calculated one-particle excitation spectra consist of a series of multiple poles and incoherent background. We assume in this approximation that the former are represented by Lorentzian peaks and the latter is neglected. The hole Green's function in vacuum is given as

$$g^R(k;t-t') = -i\sum_a z_k^a e^{(-i\epsilon_k^a-\Gamma_k^a)(t-t')}\theta(t-t'), \quad \text{(A1)}$$

where a superscript a identifies a peak, and z_k^a, ϵ_k^a, and Γ_k^a are the weight, the energy, and a damping factor of peak a with momentum k, respectively. In the same manner, the magnon Green's function defined in vacuum is given as

$$d^R(q;t-t') = -ie^{(-i\omega_q-\eta)(t-t')}\theta(t-t'), \quad \text{(A2)}$$

where ω_q and η are the energy and a damping factor of the magnon, respectively.

In this approximation, $G_3^R(k;\omega,t')$, introduced in Eq. (22), is explicitly obtained as

$$G_3^R(k;\omega,t') = \sum_{a,b,c,d}\sum_{\sigma=\pm1}\frac{\sigma C_{abcd}}{-\epsilon_{k_0}^c+\epsilon_{k_0}^d-\sigma\omega_{q=0}-i\left(\Gamma_{k_0}^c+\Gamma_{k_0}^d-\eta\right)} \times\frac{1}{\omega-\epsilon_k^a+i\Gamma_k^a}$$

$$\times \left\{ \frac{\exp\left[i\left(\epsilon^c_{k_0}-\epsilon^d_{k_0}\right)-\left(\Gamma^c_{k_0}+\Gamma^d_{k_0}\right)t'\right]}{\omega-\left(\epsilon^b_k-\epsilon^c_{k_0}+\epsilon^d_{k_0}\right)+i\left(\Gamma^b_k+\Gamma^c_{k_0}+\Gamma^d_{k_0}\right)} - \frac{e^{(-i\sigma\omega_{q=0}-\eta)t'}}{\omega-\left(\epsilon^b_k+\omega_0\sigma\right)+i\left(\Gamma^b_k+\eta\right)} \right\} \tag{A3}$$

$$= \sum_{a,b,c,d}\sum_{\sigma=\pm1} \frac{\sigma C_{abcd} e^{(-i\sigma\omega_{q=0}-\eta)t'}}{\omega-\epsilon^a_k+i\Gamma^a_k} \times \frac{D^\sigma_b\left(\omega,\Omega^\sigma_{cd},t'\right)-D^\sigma_b(\omega,0,t')}{\Omega^\sigma_{cd}}, \tag{A4}$$

where

$$D^\sigma_b(\omega,z,t') = \frac{e^{izt'}}{\omega-\left(\epsilon^b_k+\sigma\omega_{q=0}\right)+i\left(\Gamma^b_k+\eta\right)-z} \tag{A5}$$

and

$$\Omega^\sigma_{cd} = -\epsilon^c_{k_0}+\epsilon^d_{k_0}-\omega_0\sigma-i\left(\Gamma^c_{k_i}+\Gamma^d_{k_0}-\eta\right). \tag{A6}$$

We also obtain $G^R_4(k;\omega,t')$, introduced in Eq. (23), as

$$G^R_4(k;\omega,t') = \sum_{a,b,c,d}\sum_{\sigma=\pm1} \frac{-\sigma\widetilde{C}^\sigma_{abcd}}{\omega-\epsilon^a_k+i\Gamma^a_k} \times \frac{e^{\{i(\epsilon^c_{k_0}-\epsilon^d_{k_0})-(\Gamma^c_{k_0}+\Gamma^d_{k_0})\}t'}}{\omega-\left(\epsilon^b_k-\epsilon^c_{k_0}+\epsilon^d_{k_0}\right)+i\left(\Gamma^b_k+\Gamma^c_{k_0}+\Gamma^d_{k_0}\right)} \times \frac{1}{\omega-\left(\epsilon^d_{k_0}+\sigma\omega_{k-k_0}\right)+i\left(\Gamma^d_{k_0}+\eta\right)}. \tag{A7}$$

Poles in $\mathrm{Im}g^R(k;\omega)$ are labeled by indices a, b, c, and d. We introduce the constants

$$C_{abcd} = \frac{M_{k0}M_{k_00}}{2} z^a_k z^b_k z^c_{k_0} z^d_{k_0} \tag{A8}$$

and

$$\widetilde{C}^\sigma_{abcd} = \frac{M^2_\sigma}{2} z^a_k z^b_k z^c_{k_0} z^d_{k_0}, \tag{A9}$$

with

$$M_{\sigma=1} = M_{k,k-k_0}, \tag{A10}$$

$$M_{\sigma=-1} = M_{k_0,k_0-k}. \tag{A11}$$

The index σ represents the direction of the magnon propagator, i.e., $\sigma=1$ for $d(q,t)$ and $\sigma=-1$ for $d^*(q,t)$, and we have

$$d(0;t)+d^*(0;t) = \sum_{\sigma=\pm1}(-i)\sigma e^{(-i\omega_0\sigma-\eta)t}. \tag{A12}$$

We note that G^R_3 and G^R_4 cancel with each other, when $t'=0$ and $k=k_0$.

Poles in $G_3(k;\omega,t')$ and $G_4(k;\omega,t')$ are classified as the following three types:

(i) $\omega=\epsilon^a-i\Gamma^a$, originating from the poles in $g^R(k;\omega)$.

(ii) $\omega=(\epsilon^b+\omega_q\sigma)$, representing "magnon side peaks." These peaks oscillate by a factor $e^{(-i\sigma\omega_{q=0}-\eta)t'}$ and are characterized by a period $T_{\mathrm{sb}}=2\pi/\omega_{q=0}$.

(iii) $\omega=(\epsilon^b-\epsilon^c+\epsilon^d)-i(\Gamma^b+\Gamma^c+\Gamma^d)$, termed "exchange peaks." The time evoluton of these peaks is dominated by the factor $\exp[-i\{(\epsilon^c_{k_0}-\epsilon^d_{k_0})-(\Gamma^c_{k_0}+\Gamma^d_{k_0})\}t']$. Decay and oscillations are governed by $\tau_{\mathrm{decay}}=1/(\Gamma_c+\Gamma_d)$ and $T_{\mathrm{ex}}=2\pi/(\epsilon_c-\epsilon_d)$, respectively, when the transition occurs between different bands ($c\neq d$).

As shown in Fig. 7, with decreasing J, the damping rate τ_{decay} decreases. When τ_{decay} is smaller than the period T_{ex}, the exchange peaks decay rapidly. On the other hand, in the case of large J where the ladder-type peaks are well separated, τ_{decay} is large, and the contribution from the exchange peaks is not negligible.

The optical conductivity spectra are also evaluated in the DPA. A part of the optical conductivity spectra, $h_{k_0,q}(t,t')$ defined in Eq. (43), is given as

$$h_{k_0,q}(t,t') = -\sum_{a,b,c} z^a_{k_0} z^b_{\bar{l}} z^c_{k_0} \sum_{\sigma=\pm1} \frac{\sigma}{2i}\exp[(i\sigma\epsilon_{ac}-\Gamma_{ac})t] \times \exp[(i\sigma\epsilon_{bc}+i\omega_q-\gamma_{bc}-\eta)(t-t')], \tag{A13}$$

where $\bar{l}=k_0-q$, $\epsilon_{ac}=\epsilon^a_{k_0}-\epsilon^c_{k_0}$, $\epsilon_{bc}=\epsilon^b_{k_0-q}-\epsilon^c_{k_0}$, $\Gamma_{ac}=\Gamma^a_{k_0}+\Gamma^c_{k_0}$, and $\gamma_{bc}=\Gamma^b_{\bar{l}}-\Gamma^c_{k_0}$. A Fourier transform of $h_q(t,t')$ in terms of $t-t'$ is obtained as

$$h_{k_0,q}(\omega,t) = \sum_{abc}\frac{z^a_{k_0}z^b_{\bar{l}}z^c_{k_0}}{2}\sum_{\sigma=\pm1}\sigma e^{(i\sigma\epsilon_{ac}-\Gamma_{ac})t} \times \frac{\exp[(i\omega-i\sigma(\epsilon_{bc}+\omega_q)-(\gamma_{bc}+\eta))t]-1}{\omega-\sigma(\epsilon_{bc}+\omega_q)+i(\gamma_{bc}+\eta)}, \tag{A14}$$

where poles exist at $\omega=\pm(\epsilon_{bc}+\omega_q)-i(\gamma_{bc}+\eta)$. The width of the peak at finite frequencies is determined by the damping factor γ_{bc} and dispersion of the excitation energy $\epsilon_{bc}+\omega_q$. Among several terms with respect to the indices abc, contributions where a and c belong to the lowest QP band in the one-particle excitation spectra are large, because of the damping factors $e^{-\Gamma_{ac}t}$, which makes other terms small. We classify the peaks at finite frequency in the optical conductivity spectra as

(i) $b=c$, in which the peak is termed the "the side peak"; and

(ii) $b\neq c$, in which the peak is termed "the high-energy peak."

In case i, scatterings of the dynamically doped hole occur from k_0 to k_0-q inside the lowest QP band and induce a peak in the optical conductivity spectra at around $\omega=\pm(\delta\epsilon+\omega_q)$, where $\delta\epsilon$ is characterized by the band width of the hole. As a dynamically doped hole is dressed by spin clouds, $\delta\epsilon$ and the energy of the side peak increase. In case ii, transitions of the dynamically doped hole from the lowest-energy QP band to the higher-energy bands occur.

From Eq. (A14), early time dynamics in the optical conductivity spectra are estimated. By expanding the right-hand side of Eq. (A14) with respect to t, we have

$$h_{k_0,q}(\omega,t) = \sum_{abc}\frac{z_{k_{0a}}z_{\bar{l}_b}z_{k_{0c}}}{2}\epsilon_{ac}t^2+O(t^3), \tag{A15}$$

where the coefficient of $O(t^3)$ is a complex number and finite for any ω. The Drude weight, being proportional to $\mathrm{Re}[h_q(\omega=0,t)]$, obeys t^2, and the finite-frequency component $\sigma(\omega\neq0,t)$, being proportional to $\mathrm{Im}[h_q(\omega\neq0,t)]$, obeys $\propto t^3$.

[1] K. Nasu (ed.), *Photoinduced Phase Transitions* (World Scientific, Singapore, 2004), and references therein.
[2] Y. Tokura, J. Phys. Soc. Jpn. **75**, 011001 (2006).
[3] T. Oka and H. Aoki, Phys. Rev. Lett. **95**, 137601 (2005).
[4] F. Heidrich-Meisner, I. Gonzalez, K. A. Al-Hassanieh, A. E. Feiguin, M. J. Rozenberg, and E. Dagotto, Phys. Rev. B **82**, 205110 (2010).
[5] L. Vidmar, J. Bonca, T. Tohyama, and S. Maekawa, Phys. Rev. Lett. **107**, 246404 (2011).
[6] M. Mierzejewski, L. Vidmar, J. Bonča, and P. Prelovšek, Phys. Rev. Lett. **106**, 196401 (2011).
[7] J. K. Freericks, V. M. Turkowski, and V. Zlatic, Phys. Rev. Lett. **97**, 266408 (2006).
[8] B. Moritz, T. P. Devereaux, and J. K. Freericks, Phys. Rev. B **81**, 165112 (2010).
[9] P. Werner, T. Oka, M. Eckstein, and A. J. Millis, Phys. Rev. B **81**, 035108 (2010).
[10] S. G. Han, Z. V. Vardeny, K. S. Wong, O. G. Symko, and G. Koren, Phys. Rev. Lett. **65**, 2708 (1990).
[11] K. Matsuda, I. Hirabayashi, K. Kawamoto, T. Nabatame, T. Tokizaki, and A. Nakamura, Phys. Rev. B **50**, 4097 (1994).
[12] A. Cavalleri, Cs. Tóth, C. W. Siders, J. A. Squier, F. Ráksi, P. Forget, and J. C. Kieffer, Phys. Rev. Lett. **87**, 237401 (2001).
[13] S. Iwai, M. Ono, A. Maeda, H. Matsuzaki, H. Kishida, H. Okamoto, and Y. Tokura, Phys. Rev. Lett. **91**, 057401 (2003).
[14] C. Kübler, H. Ehrke, R. Huber, R. Lopez, A. Halabica, R. F. Haglund, Jr., and A. Leitenstorfer, Phys. Rev. Lett. **99**, 116401 (2007).
[15] L. Perfetti, P. A. Loukakos, M. Lisowski, U. Bovensiepen, M. Wolf, H. Berger, S. Biermann, and A. Georges, New J. Phys. **10**, 053019 (2008).
[16] A. Takahashi, H. Itoh, and M. Aihara, Phys. Rev. B **77**, 205105 (2008).
[17] N. Tsuji, T. Oka, and H. Aoki, Phys. Rev. Lett. **103**, 047403 (2009).
[18] G. De Filippis, V. Cataudella, E. A. Nowadnick, T. P. Devereaux, A. S. Mishchenko, and N. Nagaosa, Phys. Rev. Lett. **109**, 176402 (2012).
[19] H. Matsueda and S. Ishihara, J. Phys. Soc. Jpn. **76**, 083703 (2007).
[20] Y. Kanamori, H. Matsueda, and S. Ishihara, Phys. Rev. Lett. **103**, 267401 (2009).
[21] Y. Kanamori, H. Matsueda, and S. Ishihara, Phys. Rev. Lett. **107**, 167403 (2011).
[22] J. Ohara, Y. Kanamori, and S. Ishihara, Phys. Rev. B **88**, 085107 (2013).
[23] H. Okamoto, T. Miyagoe, K. Kobayashi, H. Uemura, H. Nishioka, H. Matsuzaki, A. Sawa, and Y. Tokura, Phys. Rev. B **82**, 060513 (2010); **83**, 125102 (2011).
[24] D. Golez, J. Bonca, M. Mierzejewski, and L. Vidmar, arXiv:1311.5574.
[25] Z. Hiroi, T. Yamauchi, Y. Muraoka, T. Muramatsu, and J. Yamamura, J. Phys. Soc. Jpn. **72**, 3049 (2003).
[26] Y. Muraoka and Z. Hiroi, J. Phys. Soc. Jpn. **72**, 781 (2003).
[27] H. Yada, M. Matsubara, H. Yamada, A. Sawa, H. Matsuzaki, and H. Okamoto, Phys. Rev. B **83**, 165408 (2011).
[28] H. Yada, M. Matsubara, H. Matsuzaki, H. Yamada, A. Sawa, and H. Okamoto, Phys. Rev. B **84**, 045114 (2011).
[29] J. Rammer, *Quantum Field Theory of Non-equilibrium States* (Cambridge University Press, Cambridge, UK, 2007).
[30] A. Kamanev, *Field Theory of Non-equilibrium Systems* (Cambridge University Press, Cambridge, UK, 2011).
[31] G. Stefanucci and R. van Leeuwen, *Non-equilibrium Many-Body Theory of Quantum Systems* (Cambridge University Press, Cambridge, UK, 2013).
[32] C. L. Kane, P. A. Lee, and N. Read, Phys. Rev. B **39**, 6880 (1989).
[33] G. Martínez and P. Horsch, Phys. Rev. B **44**, 317 (1991).
[34] D. Polli, M. Rini, S. Wall, R. W. Schoenlein, Y. Tomioka, Y. Tokura, G. Cerullo, and A. Cavalleri, Nat. Mater. **6**, 643 (2007).
[35] D. A. Mazurenko, A. A. Nugroho, T. T. M. Palstra, and P. H. M. van Loosdrecht, Phys. Rev. Lett. **101**, 245702 (2008).
[36] P. Beaud, S. L. Johnson, E. Vorobeva, U. Staub, R. A. De Souza, C. J. Milne, Q. X. Jia, and G. Ingold, Phys Rev Lett. **103**, 155702 (2009).
[37] H. Ichikawa, S. Nozawa, T. Sato, A. Tomita, K. Ichiyanagi, M. Chollet, L. Guerin, N. Dean, A. Cavalleri, S. Adachi, T. Arima, H. Sawa, Y. Ogimoto, M. Nakamura, R. Tamaki, K. Miyano, and S. Koshihara, Nat. Mater. **10**, 101 (2011).
[38] N. Maeshima, K. Hino, and K. Yonemitsu, Phys. Rev. B **82**, 161105(R) (2010).
[39] F. Mack and P. Horsch, Phys. Rev. Lett. **82**, 3160 (1999).
[40] S. Ishihara, Phys. Rev. Lett. **94**, 156408 (2005).
[41] K. Wohlfeld, A. M. Oles, and P. Horsch, Phys. Rev. B **79**, 224433 (2009).
[42] J. Nasu and S. Ishihara, Phys. Rev. B **88**, 205110 (2013).
[43] N. M. Plakida, V. S. Oudovenko, and V. Yu. Yushankhai, Phys. Rev. B **50**, 6431 (1994).